3
Drill-string experimental set-up

According to [83], the experiments may be traditionally grouped in three categories: 1°) the experiments performed to primarily improve the understanding of some physical phenomenon; 2°) the experiments primarily for parameter determination to base a mathematical model of a well known physical phenomenon; and 3°) the experiments to determine reliability, performance, or safety of components. Herein, the test bench and the experiments of this thesis belong to the first category. That is so because a better understanding of stick-slip phenomenon in slender structure as well as the strategy to mitigate/eliminate this phenomenon is sought. This experimental slender structure was designed to simulate a drill-string in reduced scale.

Only few works present the details for the development of test bench simulating a drilling system. Some relevant test rigs are described in [18, 43, 44, 48, 59, 84–86]. Also, the author of this thesis described a two degree of freedom horizontal set-up in order to study dry friction-induced torsional vibrations and stick-slip phenomenon in 2013 [15]. Until that moment, no experimental apparatus of this kind had been constructed in Brazil. During studies and conclusions, some modifications were made to enhance the test bench and to investigate interesting situations, as proposed in Section 1.2.

Firstly, the operational description of the test bench, sensors and parameter identifications are performed. Subsequently, the brake device is addressed in order to point the mechanism of dry friction that induces torsional oscillations. Ending this chapter, a summary with the remarks is accomplished. The `LabView` software and the `Python 3.6` language are used for data acquisition and post-processing along this thesis.

3.1
Description of the experimental set-up

The test rig consists of a system with three discs: Disc 1 (R_1), Disc 2 (R_2) and the DC-motor inertia (R_3): R_1 is placed on the opposite extremity of the DC-motor, and the second one R_2 is intermediary placed. Resistive torques may be independently applied on both discs and the behavior of the system is

analyzed. It is fully instrumented consequently it is possible to observe torsional vibrations and the stick-slip phenomenon when a friction torque is applied on R_1 and during this stick-slip, another friction torque may be applied on R_2. A low-stiffness shaft (2.40 m length and 3 mm diameter) is responsible to transmit rotation from DC-motor to the discs (see Figure 3.1). The discs are free to rotate around their geometric center, and their lateral motions are constrained by bearings. This DC-motor is an *ENGEL GNM 5480-G6.1* of series *E*, as depicted in Figure 3.1(c). This DC-motor presents a planetary gearbox relation 8:1 and an internal PI controller in order to control the angular velocity in R_3. The parameters of the electrical subsystem were taken from the manual of the DC-motor and described in Table 3.1.

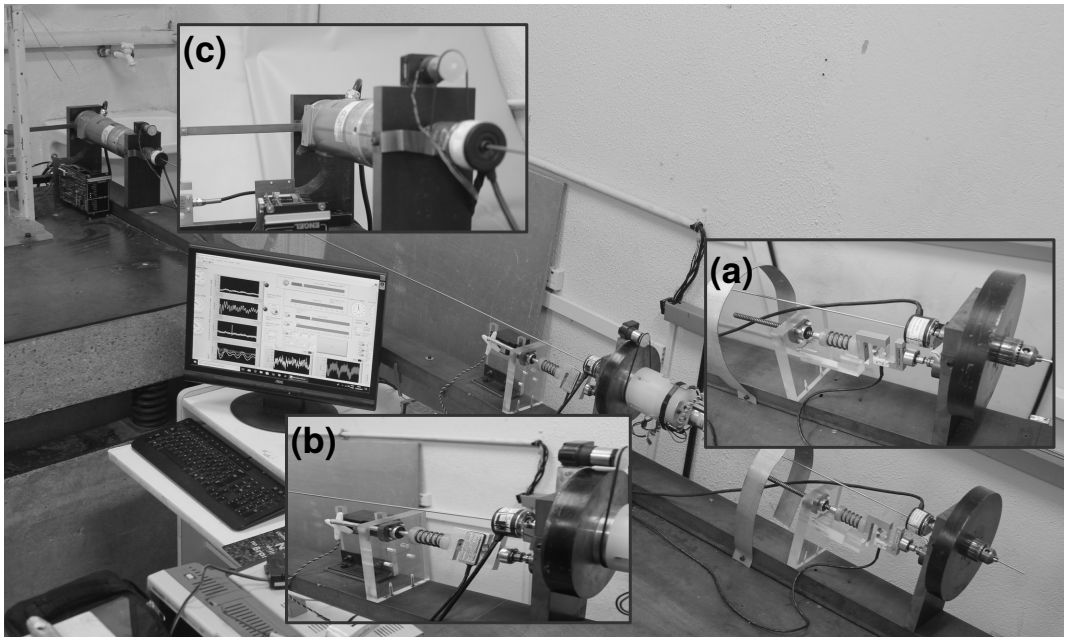

Figure 3.1: Drill-string experimental set-up. (a) Disc 1 (R_1) and brake device 1, (b) Disc 2 (R_2) and brake device 2 and (c) DC-motor [87].

The brake devices consist of pins that pass through the bearing support and come in contact with the discs R_1 and R_2. This dry contact generates a friction torque leading to torsional vibration (or even stick-slip). The normal forces (N_1 and N_2) created by contact of the pins with the discs are acquired by force sensors. For the torque source on R_2, there is a servo motor responsible for moving the pin (active torque). The mitigation strategy is based on this mechanical component. Figure 3.2 illustrates the components located on R_1 and R_2, while Figure 3.3 shows a scheme of the experimental set-up. In this later figure one may also observe the operation of the friction device.

Comparing the diameter/length of slender structures, one may observe that this experimental apparatus presents $D/L = 0.0013$, whereas the drill-

Table 3.1: Electrical parameters of DC-motor.

Parameter	Description	Value	Unit
L	armature inductance	$8.437 \cdot 10^{-4}$	H
R	armature resistance	0.33	Ω
K_T	torque constant	0.126	Nm/A
K_E	voltage constant	0.0602	$V/(rad/s)$
T_f	friction torque	0.1196	Nm
C_m	speed regulation constant	$1.784 \cdot 10^{-4}$	$Nm/(rad/s)$
k_p	proportional constant	2.800	–
k_i	integral constant	3.500	–
J_m	moment of inertia	$0.370 \cdot 10^{-3}$	$kg\,m^2$
η	transmission factor	8	–

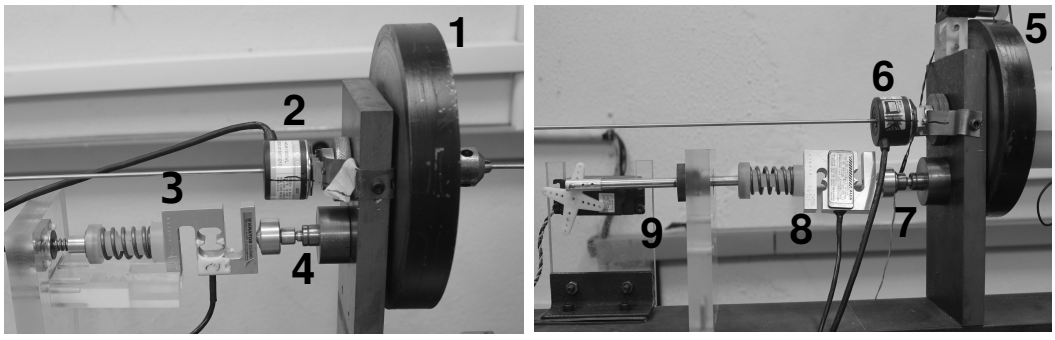

(a) (b)

Figure 3.2: Discs, brake devices and measure components: 1, 5 - the discs R_1 and R_2; 2, 6 - incremental encoders; 3, 8 - load cells; 4, 7 - contact pins; 9 - servo motor [87].

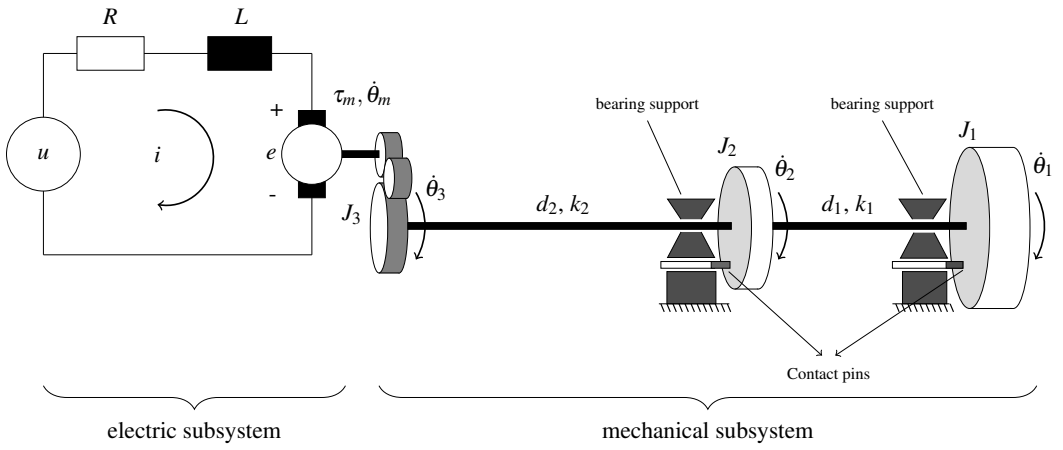

Figure 3.3: Schematic diagram of the test bench. Adapted from [68].

string system approached in [69] (4733.6 m length and 0.140 m outer diameter) presents $D/L = 0.0003$. This means that a full scale drill-string is even more slender than the reduced scale drill-string of this thesis, and this justifies the chosen dimensions.

3.1.1 Sensors and instrumentation

Incremental encoders were used to acquire the angular speed at discs R_1, R_2 and DC-motor R_3 – *LS Mecapion* of 1000 ticks/revolution, as depicted in Figure 3.4(a). The friction forces are measured by load cells S10 R9 255 from *Kratos equipamentos* at R_1 and SV50 R-5 from *Alpha Instrumentos* at R_2 (see Figure 3.4(b)-(c)). The distances between the contact points and the rotation centers of the discs r_i $(i = 1, 2)$ are known. The applied DC-motor torque is acquired by a load cell CSL/ZL-20 from *MK Controle e Instrumentação*. As in [15, 42], the DC-motor is mounted on two bearings: the motor applies torque and the system reacts with the same magnitude. Thereby the reactive torque from the system on the motor is acquired. Figure 3.4(b) shows the force sensor and measurement schema of the torque from DC-motor.

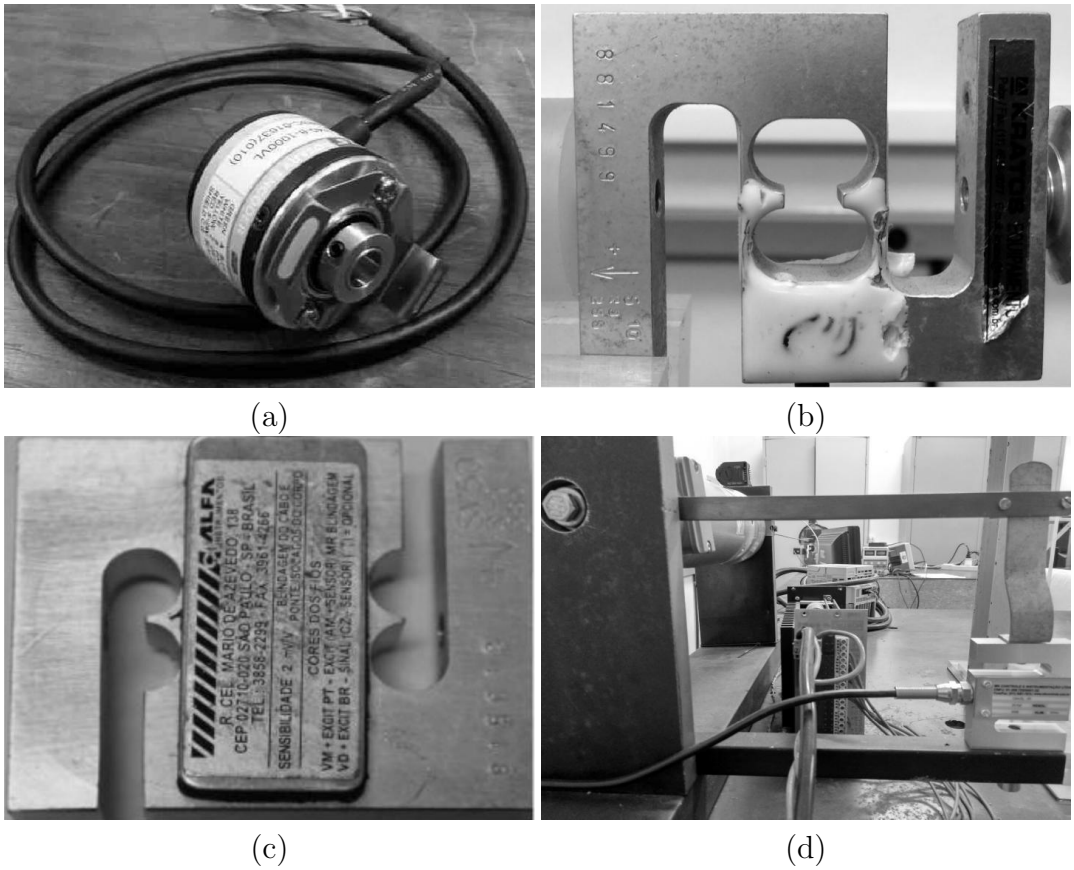

Figure 3.4: Measurement equipment: (a) incremental encoder, (b) load cell at R_1, (c) load cell at R_2, and (d) schema of the DC-motor torque measurement and the load cell.

In order to perform acquisition and record of the data, the cDAQ-9174 USB with four slots from *National Instruments*, see Figure 3.5(a), was used with a sampling time of 10 *ms* (*milliseconds*). The software `LabView` was employed to provide user-board-sensors interface. The servo controller

responsible for an active torque on R_2 is depicted in Figure 3.5(b): it is a CS-80 GIANT-SCALE 2BB SERVO from *Hobbico*.

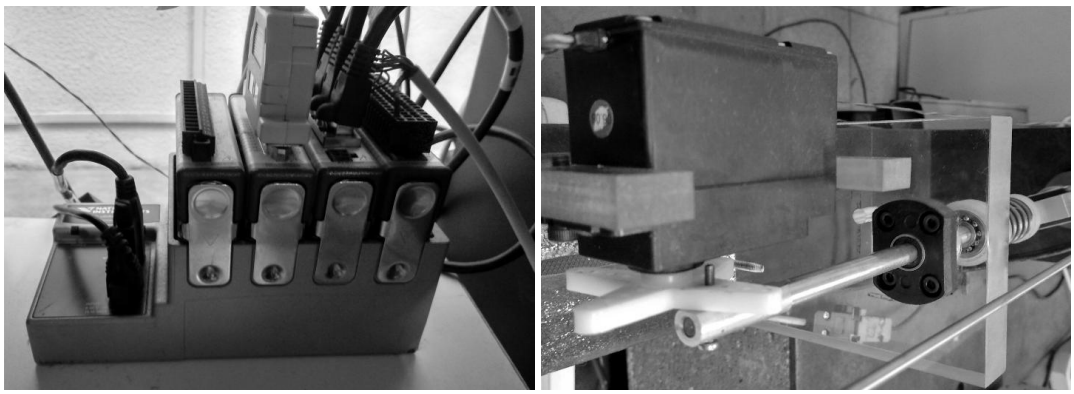

(a) (b)

Figure 3.5: Experimental components: (a) acquisition device and (b) servo controller.

3.1.2 Parameter identification

The parameters of the experimental set-up must be identified in order to achieve representativity of the equations of motion.

– *Identification of the moments of inertia.* The discs were considered rigid and their weights were recorded (see Figure 3.2). For characterization of the moments of inertia, the following relation was used

$$J_i = \frac{1}{2} m_i \left(\frac{D_i}{2} \right)^2, \tag{3-1}$$

where m_i and D_i represent the mass and diameter of the discs ($i = 1, 2$), respectively. Table 3.2 contains the calculated values.

Table 3.2: Moments of inertia of the discs.

i	$m_i\,[\,kg\,]$	$D_i\,[\,m\,]$	$J_i\,[\,kg\,m^2\,]$
1	6.40	0.190	0.02888
2	4.56	0.162	0.01496

– *Identification of the stiffnesses.* Initially, it was performed a static test with known weight applied tangentially to the discs and the angular displacement was acquired in order to identify k_1 and k_2 (see Figure 3.3). Figure 3.6(a) illustrates the results of k_1 and Figure 3.6(b) comprises the results of k_2.

It is important to remark that the amplitudes of angular displacements occur in the linear region of the string. The Hooke's law was used to calculate

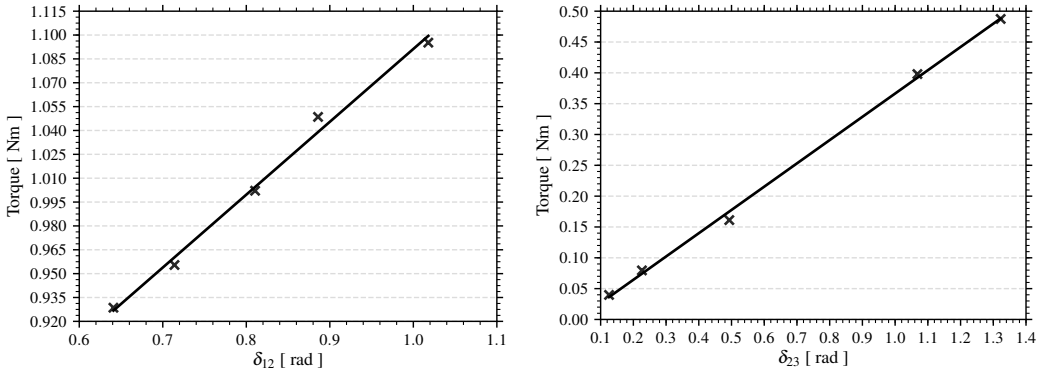

(a) (b)

Figure 3.6: Relation between torque and angular displacement.

the stiffnesses k_1 and k_2. The results of the static test is described in Table 3.3. Equation (3-2) is used to calculate the stiffnesses

$$g\,W_j\,\frac{D_1}{2} = k_{1_j}\,\delta_{12_j}, \qquad g\,W_j\,\frac{D_2}{2} = k_{2_j}\,\delta_{23_j}, \tag{3-2}$$

where $g = 9.81\,m/s^2$ as the gravity and W_j is the jth weight in kg, and j means the number of test. The D_1 and D_2 denote the diameters, as used in Eq. (3-1). The δ_{12} and δ_{23} are the angular displacements between discs 1 and 2, and discs 2 and 3 in rad, respectively, *i.e.*, $\delta_{12} = \theta_1 - \theta_2$ and $\delta_{23} = \theta_2 - \theta_3$.

Table 3.3: Static test and stiffness estimations.

j	Torque$_j$ [Nm]	δ_{12_j} [rad]	k_{1_j} [Nm/rad]
1	0.9286	0.6409	1.4489
2	0.9554	0.7140	1.3381
3	1.0021	0.8105	1.2364
4	1.0485	0.8859	1.1835
5	1.0952	1.0179	1.0759
mean			1.2566
j	Torque$_j$ [Nm]	δ_{23_j} [rad]	k_{2_j} [Nm/rad]
1	0.0398	0.1257	0.3168
2	0.0795	0.2262	0.3516
3	0.1611	0.4932	0.3267
4	0.3980	1.0681	0.3726
5	0.4874	1.3226	0.3685
mean			0.3473

Thereafter, the angular velocities $\dot{\theta}_i$ $(i = 1, 2, 3)$ were acquired and in Figure 3.7 it is shown the time and frequency responses of the test rig. The DC-motor was turned on to provide 30 rpm and then a disturbance was imposed by

hand. This figure also provides $\omega_{n_1} = 0.396\,(2\,\pi)$ [rad/s] and $\omega_{n_2} = 1.781\,(2\,\pi)$ [rad/s].

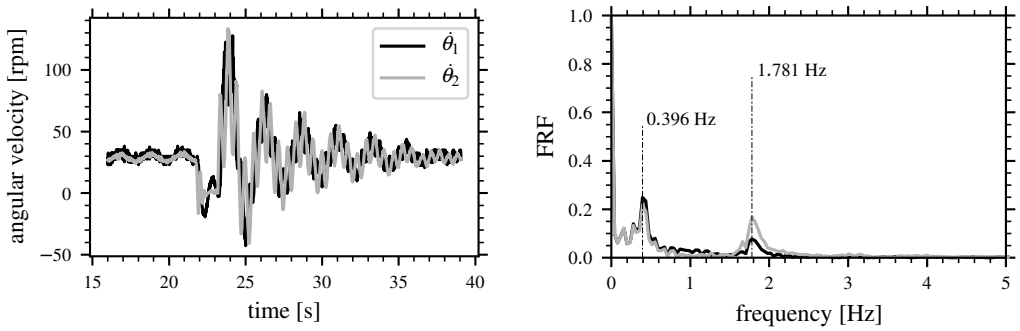

(a) (b)

Figure 3.7: Measured data of a free vibration around 30 rpm from test rig. In (a) time response and (b) frequency response function.

Subsequently, the mechanical undamped model of the system is considered, as illustrated in Figure 3.8. Therewith, the system may be described as follows

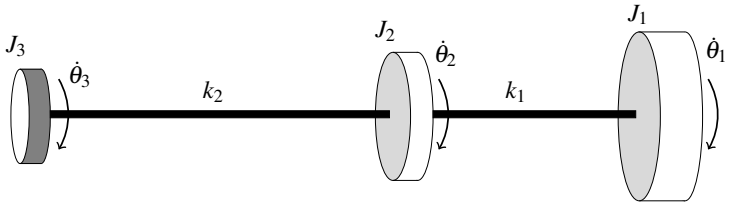

Figure 3.8: Mechanical model of the test rig.

$$\begin{bmatrix} J_1 & 0 & 0 \\ 0 & J_2 & 0 \\ 0 & 0 & J_3 \end{bmatrix} \begin{bmatrix} \ddot{\theta}_1 \\ \ddot{\theta}_2 \\ \ddot{\theta}_3 \end{bmatrix} + \begin{bmatrix} k_1 & -k_1 & 0 \\ -k_1 & k_1 + k_2 & -k_2 \\ 0 & -k_2 & k_2 \end{bmatrix} \begin{bmatrix} \theta_1 \\ \theta_2 \\ \theta_3 \end{bmatrix} = \begin{bmatrix} 0 \\ 0 \\ 0 \end{bmatrix}, \qquad (3\text{-}3)$$

where $J_3 = \eta^2 J_m$ (see Table 3.1). Equation (3-3) leads to a characteristic polynomial

$$\lambda\,(a\lambda^2 + b\,\lambda + c) = 0. \qquad (3\text{-}4)$$

Equation (3-4) provides three roots: one of them is $\lambda = 0$, which means the rigid body motion and the others are

$$\lambda_1 = \frac{-b - \sqrt{b^2 - 4ac}}{2a}, \qquad \lambda_2 = \frac{-b + \sqrt{b^2 - 4ac}}{2a}. \qquad (3\text{-}5)$$

From Eq. (3-5), the parameters a, b, and c are functions of the unknown stiffnesses k_1 and k_2. Hence, the stiffnesses were identified via *root* command

from `Python`. This function possesses several options to find the roots of a nonlinear function. The *modified Powell method* [88] was herein employed. The objective function may be written as follows

$$f(k_1, k_2) = \left[\omega_{n_1}^2 - \lambda_1, \omega_{n_2}^2 - \lambda_2\right], \tag{3-6}$$

and when $f(k_1, k_2) = [0, 0]$, it leads to

$$\begin{aligned} k_1 &= 1.1175 \quad [\text{ Nm/rad }], \\ k_2 &= 0.3659 \quad [\text{ Nm/rad }]. \end{aligned} \tag{3-7}$$

The solution of the Eq. (3-6) is possible because the moments of inertia are known (see Tables 3.1 and 3.2) and the initial points were the mean stiffnesses values obtained in the static test (see Table 3.3). One may notice that the stiffnesses values of the static (Table 3.3) and dynamic testes (Eq. (3-7)) are slight different: this might happen because of an inner friction of ball bearings (disc supports) and the influence of DC-motor dynamics which was unconsidered.

– *Identification of the damping.* The damping coefficients were found by acquiring experimentally the free time responses of the system, as shown in Figure 3.9. It is worth to mention that the disc R_2 was restricted to rotate and therewith the free oscillation of $\dot{\theta}_1$ was acquired, as depicted in Figure 3.9(a). Likewise, the disc R_1 was restricted to rotate, thereat the free oscillation of $\dot{\theta}_2$ was recorded. This latter is illustrated in Figure 3.9(b). The peaks were noted for computing the damping ratio ξ. To do so, it was used the logarithmic decrement as follows in Eq. (3-8)

$$\xi_i = \frac{1}{\sqrt{1 + \left(\frac{2\pi}{ln(x_{p_j}/x_{p_{j+1}})}\right)^2}} \quad \text{for} \quad i = 1, 2\,, \tag{3-8}$$

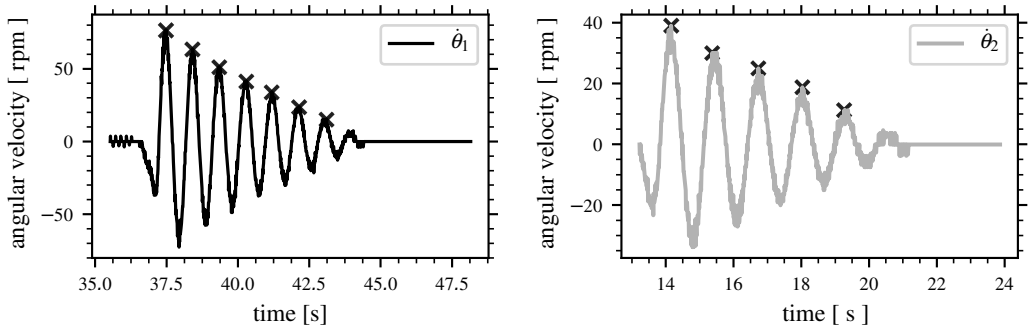

(a) (b)

Figure 3.9: Free time response of (a) disc 1 and (b) disc 2.

where x_{p_j} and $x_{p_{j+1}}$ are the jth and $jth+1$ amplitudes peaks, respectively. Table 3.4 contains the estimation of the damping ratio ξ_i.

Table 3.4: Damping ration estimation.

j	ξ_{1_j} $[-]$	ξ_{2_j} $[-]$
1	0.05698	0.05574
2	0.05817	0.05418
3	0.05351	0.05266
mean	0.05622	0.05419

Thereby, the damping coefficients are calculated via Eq. (3-9), using the moments of inertia from Table 3.2 and the stiffnesses estimated by Eq. (3-7),

$$\begin{aligned} d_1 &= 2\,\xi_1\,\sqrt{k_1\,J_1} = 0.02145 \quad [\,Nm\,s/rad\,] \\ d_2 &= 2\,\xi_2\,\sqrt{(k_1+k_2)\,J_2} = 0.01595 \quad [\,Nm\,s/rad\,]. \end{aligned} \tag{3-9}$$

– *Identification of the static friction coefficient.* The friction created by the contact pin (see Figure 3.3) is modeled as a dry friction which possesses a static and kinetic coefficients of friction. In order to identify the static friction coefficient, a simple test may be performed: the normal force N_1 generated by the pin is applied at a known distance r_1, as described in [15, 41]. Subsequently, a dynamometer tangentially measures the needed force to overcome the resistive torque created by the pin. Thereby, the friction may be achieved μ_s following

$$\mu_s = \frac{F_T \cdot D_1/2}{N_1 \cdot r_1}, \tag{3-10}$$

where F_T denotes the tangential force and $r_1 = 0.047\ m$ is the distance between the contact point of the pin and the geometric center of rotation of disc R_1. Table 3.5 presents the experimental trials for the static friction identification.

Table 3.5: Identification of the static friction coefficient.

N_1	F_T	μ_s	N_1	F_T	μ_s	N_1	F_T	μ_s
6.10	1.40	0.4639	9.50	2.30	0.4894	15.70	3.90	0.5021
6.15	1.55	0.5094	9.55	2.40	0.5080	15.65	3.85	0.4972
6.00	1.50	0.5053	9.50	2.40	0.5106	15.60	3.80	0.4924
6.20	1.60	0.5216	9.40	2.25	0.4838	15.70	3.95	0.5085
6.15	1.55	0.5094	9.65	2.35	0.4922	15.75	3.80	0.4877
mean:		0.5019	mean:		0.4968	mean:		0.4976

Therewith, the value adopted was the mean of the mean values described in Table 3.5, as follows

$$\mu_s = \frac{0.5019 + 0.4968 + 0.4976}{3} \approx 0.5. \tag{3-11}$$

– *Identification of the kinetic friction coefficient.* Firstly, the disc R_1 is loose from the string and an initial condition of rotation was given by hand. Then the contact force was imposed. The equation that represents this situation is

$$J_1\,\ddot{\theta}_1 + T_{r_1}(\dot{\theta}_1) = 0, \tag{3-12}$$

where the $T_{r_1}(\dot{\theta}_1)$ is the resistive torque created by the pin. This torque is modeled as a velocity-dependent friction as follows [42–44, 48, 89, 90]

$$T_{r_1}(\dot{\theta}_1) = N_1\, r_1 \left[\mu_k + (\mu_s - \mu_k)\, e^{-|\dot{\theta}_1|}\right]. \tag{3-13}$$

The normal force N_1 and the angular velocity $\dot{\theta}_1$ are acquired, whereas μ_s, r_1, and J_1 are known. The angular acceleration $\ddot{\theta}_1$ is obtained via an estimation using the incremental encoder - considering constant angular acceleration during the acquisition time and then a discrete derivation may be applied. Figure 3.10 depicts the measured angular velocity $\dot{\theta}_1$ over time to the situation described by Eq. (3-12). One may also observe the noise from the acquire data, but this is because of the derivation procedure to estimate angular velocity.

Thereby, a least square method [91] from *scipy.optimize* (`Python`) was applied to the system described by Eq. (3-12) in order to estimate the unknown kinetic friction coefficient μ_k. The estimated value of kinetic friction coefficient is

$$\mu_k = \frac{0.340 + 0.292 + 0.293 + 0.302}{4} = 0.306. \tag{3-14}$$

Some experimental trials showed inconsistent values and were unconsidered.

3.2 Development of the dry friction device

Keeping in mind the financial limitations, the brake device pursues the idea of efficiency and low cost, *i.e.*, phenomena representation with feasibility. Therewith, the device used to create dry friction-induced vibration has been changed over time. Following, the friction device evolution is described.

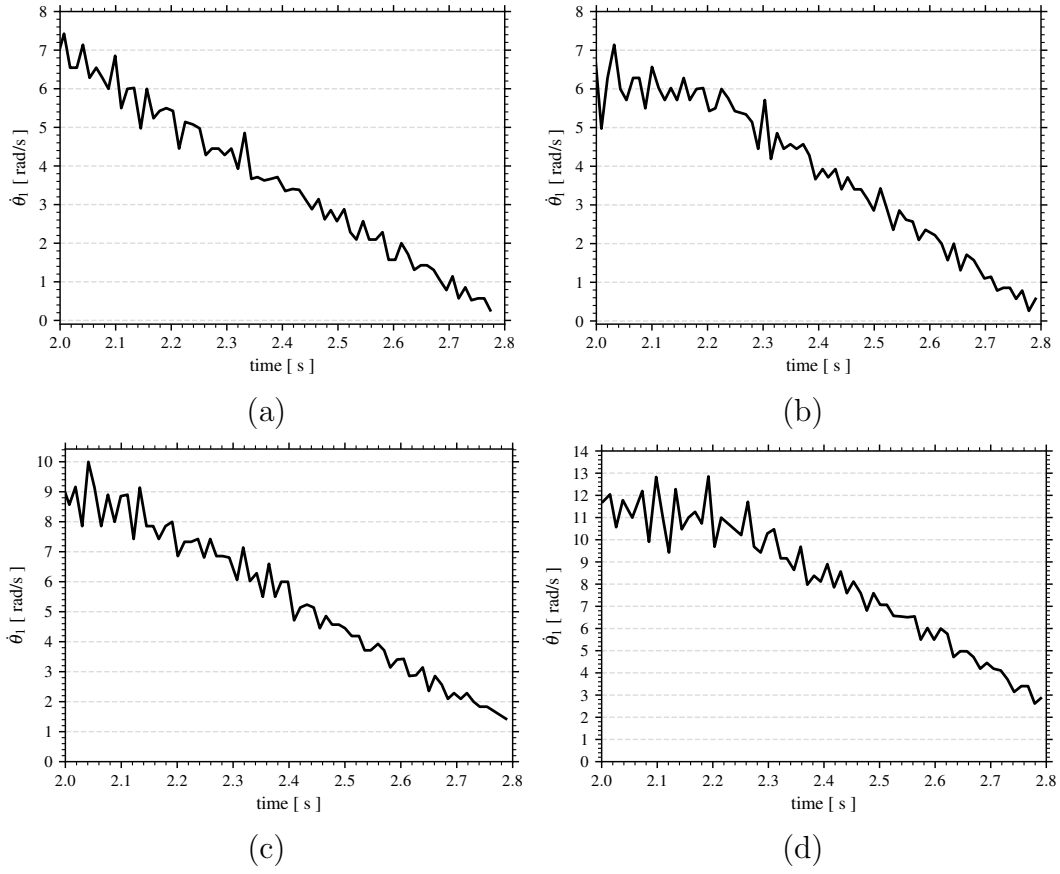

Figure 3.10: Angular speed of the Disc 1 (R_1) to given a rotation and applied resistive torque. In (a) $\mu_k = 0.358$, (b) $\mu_k = 0.322$, (c) $\mu_k = 0.349$, and (d) $\mu_k = 0.342$.

3.2.1
First device: bicycle brake

The former device was composed of brake pads and a brake disc of bicycles. The former is responsible to induce dry friction via contact material. The later was acceded to the R_1, keeping the same angular speed. Figure 3.11(a) depicts the R_1 and the brake disc, whereas Figure 3.11(b) shows the device which imposes a contact force on the radial end of the brake disc creating a resistive torque to the rotational motion of the R_1 [15]. A servo controller was located on the load cell which was responsible for the opening/closing actuation of the pads. This load cell was responsible to measure indirectly the resistive torque on R_1.

This first device was successfully used in [15, 40, 92] to observe stick-slip phenomenon in the drill-string experimental set-up, meeting the problem physics and the resource requirements.

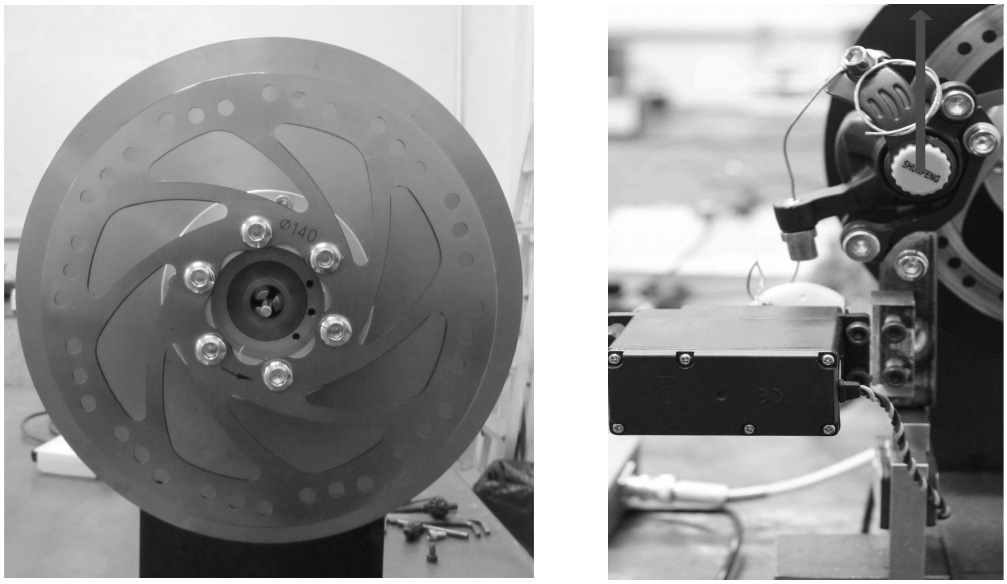

(a) (b)

Figure 3.11: First device: (a) brake disc and R_1, and (b) brake pads, brake disc, load cell and servo controller [15].

3.2.2 Second device: pins

An evolution of the friction device has been developed as illustrated in Figure 3.2: the pins pass through the bearing supports and come in contact with the rotating discs. Unlike the first device, the contact force is measured directly via a load cell attached to the pins. The stick-slip phenomenon was observed in [41] (2015) and [42] (2017) using this updated device.

Figure 3.12 illustrates a workpiece which contains a ball joint responsible to connect the pin to the load cell. This component allows a better data acquisition and guarantees the normal contact of the pin with the disc.

It is worth to remark the possibility of the contact material changing in order to investigate the influence of friction coefficients on the dynamical behavior of the test bench. Figure 3.13 shows the already available pins. In this thesis, the second device is used to achieve torsional oscillations rising from the dry friction. The aluminum pin is used in this work.

An addendum about the polymer POM is that this material presents high temperature and abrasion resistances, high hardness, stiffness and toughness. It is a thermoplastic with large engineering applications such as ball bearings, gear wheels, fasteners, among others. For example in [93], this polymer is used to the rotor-bearings contact in order to avoid backward whirl. The friction and wear characterization is performed, and then the nonlinear rotor-bearing interactions is analyzed experimentally.

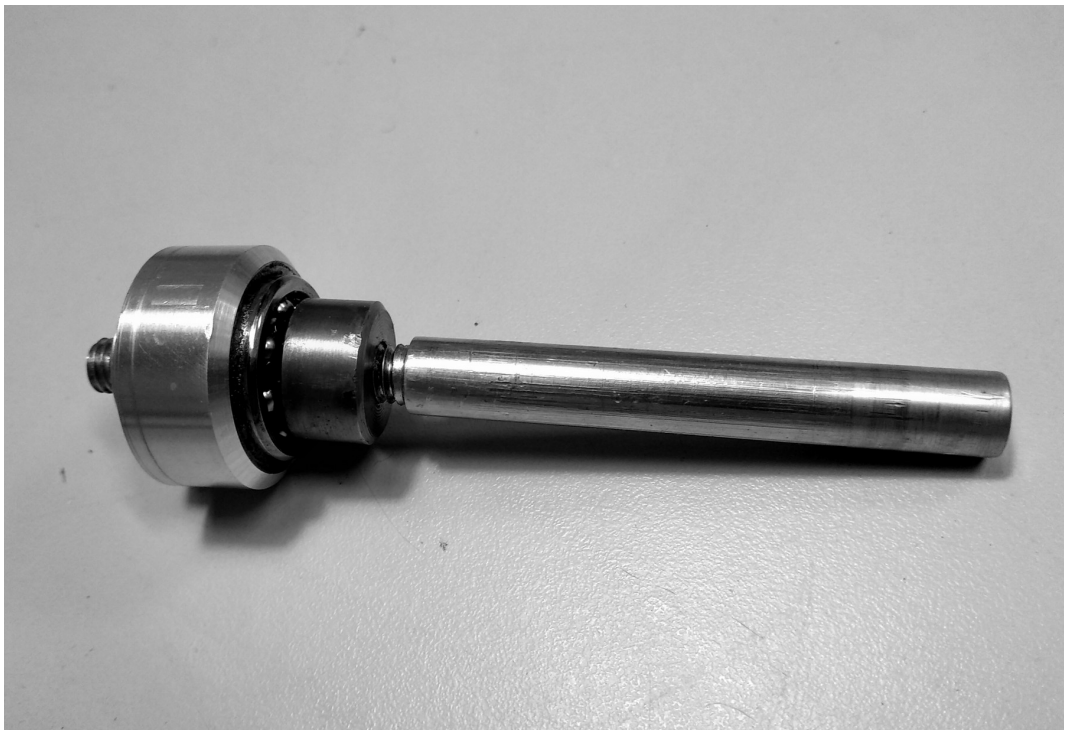

Figure 3.12: Ball joint of the pin in the second friction device.

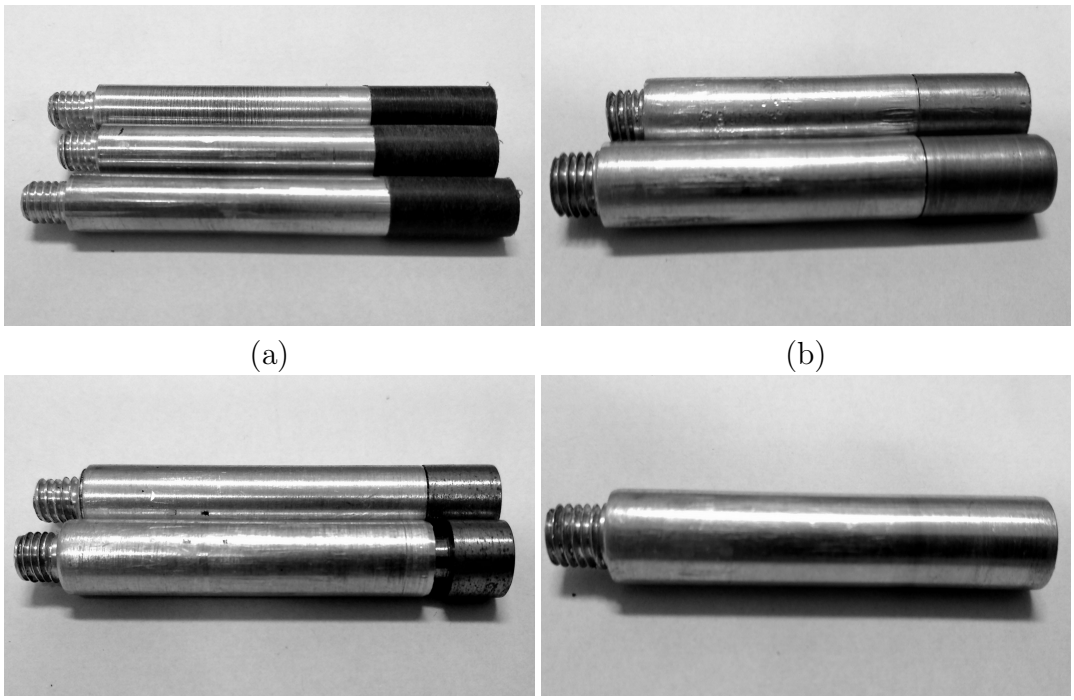

(a) (b)

(c) (d)

Figure 3.13: Manufactured pins of (a) polymer (POM), (b) brass, (c) steel, and (d) aluminum.

3.3 Summary

In this chapter, the drill-string experimental set-up was addressed. Section 3.1 contains the description of the main components of the test bench,

operation of the brake device, sensors involved, and parameter identification of the system. This latter procedure consisted of the estimation of the moments of inertia, stiffnesses, damping coefficients, and friction parameters in order to use them in mathematical modeling of the test bench. The instrumentation of the test rig provides the visualization and acquisition of torsional vibrations in its severe stage: the stick-slip phenomenon.

Although the experimental apparatus presents limitations such as no lateral and axial motions, it is worth mentioning that the drill-string experimental set-up presents similar torsional behavior compared to a full-scale system. In addition to the slender characteristic discussed in Section 3.1, the torsional natural frequencies are also close: the experimental apparatus presents [0.0, 0.396, 1.781] Hz, while a full scale drill-string used for comparison presents [0.0, 0.17, 1.11] Hz [69].

Then, the development and evolution of the dry friction device was described in Section 3.2. It is important to point out this experimental evolution (second device) which led to the results for this thesis and a better control of the applied normal force on the discs. The modifications may yield several analysis and works on friction-induced vibrations with different contact materials. In the thesis, the aluminum pin is used and is changed when it reaches an excessive wear, which may compromise the results.

The stick-slip phenomenon along with the nonlinear analysis are approached numerically in the next chapter.